Supplement of Atmos. Chem. Phys., 21, 17607–17629, 2021
https://doi.org/10.5194/acp-21-17607-2021-supplement

Supplement of

Long-term atmospheric emissions for the Coal Oil Point natural marine hydrocarbon seep field, offshore California

Ira Leifer et al.

Correspondence to: Ira Leifer (ira.leifer@bubbleology.com)

Supplemental Material

S1 The Gaussian Plume model theoretical basis

Sea surface emissions for focused bubble plumes can be described as a point source whose atmospheric plume can be modeled as a Gaussian plume (Hanna et al., 1982). The Gaussian plume model relates atmospheric emissions, E_A, to the concentration anomaly, C', relative to ambient, C, wind speed, u, and the atmospheric turbulence parameters, σ_y and σ_z, defined in a cartesian coordinate system where x is the downwind, i.e., wind direction, θ, y is the transverse direction, and z is the vertical coordinate,

$$C'(x,y,z) = E_A \frac{exp\left(\frac{-y^2}{2\sigma_y^2}\right)}{(2\pi u\sigma_z\sigma_y)}\left(exp\left(\frac{-(z-h)^2}{2\sigma_z^2}\right) + exp\left(\frac{-(z+h)^2}{2\sigma_z^2}\right) + exp\left(\frac{-(z-2(BL-h))^2}{2\sigma_z^2}\right) + exp\left(\frac{-(z+2(BL-h))^2}{2\sigma_z^2}\right)\right), \qquad \text{(S1)}$$

where h is the release height (after buoyant rise). The second exponential term represents reflection off the sea surface and assumes a non-sticky molecule, the third term represents reflection off the marine boundary layer, at height BL, and the fourth term represents re-reflection off the surface (Fig. S1). This reflection can be significant for a shallow BL, e.g., for $BL = 250$ m and $u = 2.1$ m s^{-1} the reflection contributes 10-20% of C' for 2-km downwind (Fig. S1). C' is relative to the background concentration, C, which is based on the concentrations outside the plume's edges and can include environmental gradients for distant sources.

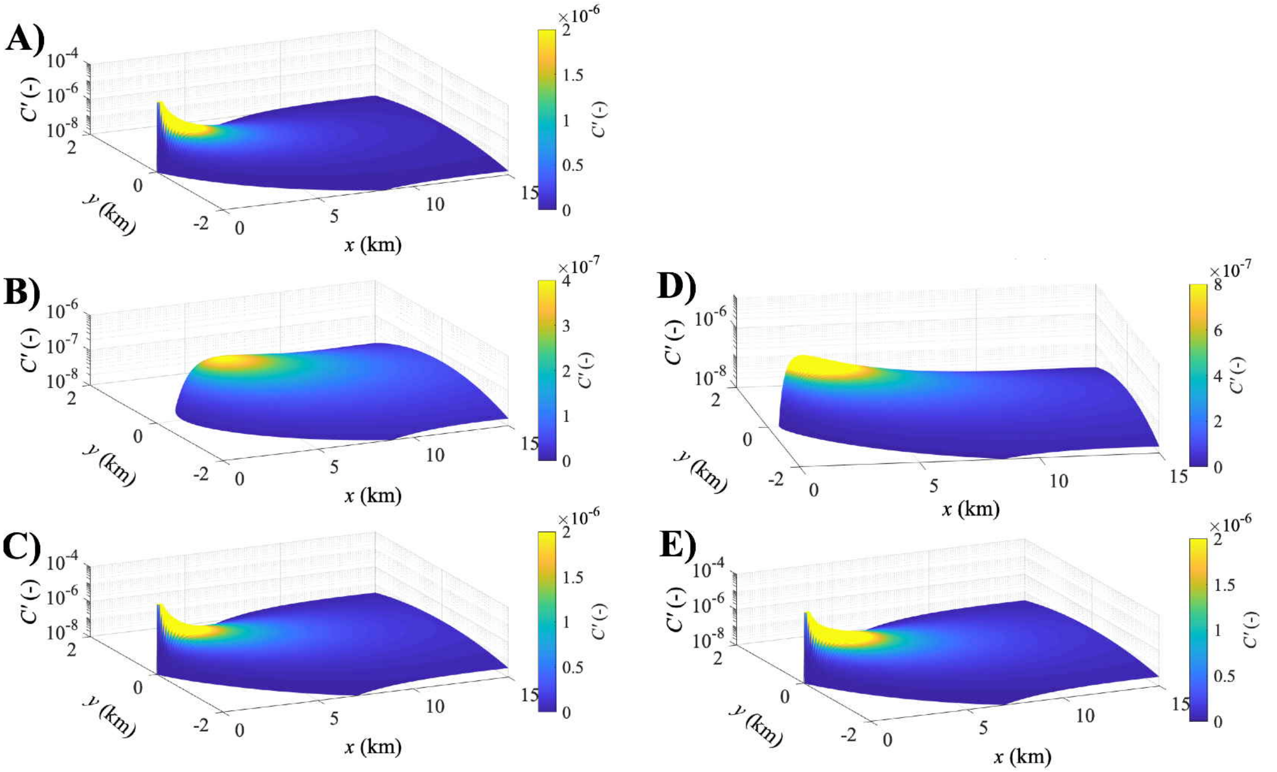

Figure S1: Surface concentration, *C'*, for Gaussian plumes for *u*=2.1 m s^{-1} **A)** with no planetary boundary layer, *BL*, **B)** reflection from a 250-m *BL* (Eqn. 1, terms 3+4) and **C)** Gaussian plume with 250-m *BL*. **D)** Reflection plume from a 100-m *BL* and **E)** Gaussian plume with 100-m *BL*. Arbitrary *C'* units. Data key on panel.

Parameterization of σ_y and σ_z are:

$$\sigma_y = a(1 + 10^{-4}x)^{-1/2}; \sigma_z = b(1 + cx)^n \ , \qquad \text{(S2)}$$

with *a*, *b*, and *c* depending on stability class (Briggs, 1973). Stability class (Table S2) is based on solar insolation, *I*, and *u* (Hanna et al., 1982). These turbulence parameterizations (Eqn. S2) are discrete (Table S1), which introduces uncertainty in σ_y and σ_z, particularly at stability class transitions. To remove discretization distortions, a 2nd-order polynomial was fit to the turbulence parameters *a*, *b*, and *c*, for each insolation class with respect to *u* (Fig. S2). The polynomial fit then was evaluated for *u* to determine *a*, *b*, and *c* for all three insolation classes. Weak, moderate, and strong insolation classes were fit for *I* = 175, 500, and 800 W m^{-2}, respectively. Given the coarse nature of the Pasquill classes, no effort was made to optimize. Instead, the center *u* for each class was used in the parameterization.

Table S1. Parameters for atmospheric turbulence parameterizations for different stability classes*

Class		*a*	*b*	*c*	*n*	Class Description
A	*open*	0.22	0.20	0	-	Extremely unstable
B	*open*	0.16	0.12	0	-	Moderately unstable
C	*open*	0.11	0.08	$2\text{x}10^{-4}$	-0.5	Slightly unstable
D	*open*	0.08	0.06	$1.5\text{x}10^{-3}$	-0.5	Neutral
E	*open*	0.06	0.03	$3\text{x}10^{-4}$	-1	Slightly stable
F	*open*	0.04	0.016	$3\text{x}10^{-4}$	-1	Moderately stable

*from Briggs (1973).

Table S2. Conditions defining Pasquill turbulence classes*

u	I_{Strong}	$I_{Moderate}$	I_{Weak}	Night	Night
m s^{-1}	>700 W m^{-2}	350-700 W m^{-2}	<350 W m^{-2}	$>{}^{1}/_{2}$ Clouds	$<{}^{3}/_{8}$ Clouds
<2	A	A-B	B	E	F
2	A-B	B	C	E	F
4	B	B-C	C	D	E
6	C	C-D	D	D	D
>6	C	D	D	D	D

*from Hanna et al. (1982). *u* is wind speed, *I* is solar insolation.

The Gaussian plume model is for a passive dispersant and assumes negligible along-wind diffusion, that u, σ_y, and σ_z are vertically and horizontally uniform along its trajectory, that *u* fluctuations are zero, and that *u* remains parallel to the *x* axis (no veering). These assumptions imply an idealized, flat terrain of homogeneous roughness. Violations of these conditions are common in terrestrial settings and can be addressed by model modification, e.g., Briggs (1973); Leifer et al. (2016), the absence of topography and obstructions at sea implies that marine plumes generally satisfy the Gaussian plume requirements.

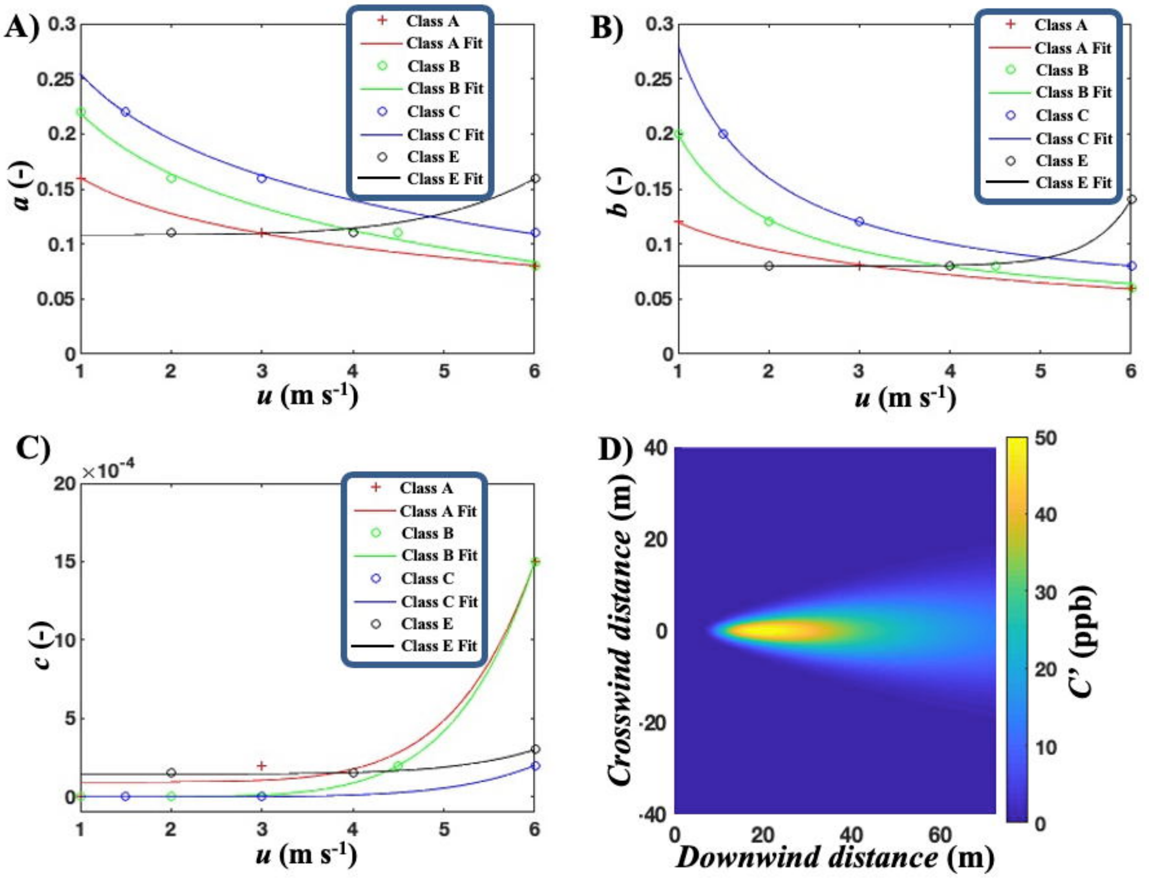

Figure S2: Pasquill turbulence parameters (Table S1) and 2nd-order polynomial least-squares linear-regression fits of A) *a*, B) *b*, and C) *c* for solar insolation stability classes (Table S1; class data key on figure) versus wind speed, *u*. See text for details. D) Gaussian plume surface concentration, C', for 0.47 L min^{-1} emissions, $u = 3.5$ m s^{-1}, and no boundary layer.

Simulations were conducted for three conditions: Infinite planetary boundary layer, i.e., no reflection, a 250-m *BL*, and a 100-m *BL*. The 250-m *BL* only affects *C'* several kilometers downwind, whereas for *BL*=100 m, the reflection affects *C'* far closer to the source and far more strongly. As the plume combines with its reflection the downwind plume *C'* flattens near the plume axis, leading to a sharper off-axis decrease in *C'*.

S2 Focused seep areas

Table S3. Location and direction from West Campus Station of informally-named seeps

Seep Area	θ	Latitude, Longitude
La Goleta Seep	152°	34° 23.503'N, 119° 51.193'W
Seep Tent Seep	198°	34° 23.063'N, 119° 53.428'W
Platform Holly	238°	34° 23.392'N, 119° 54.374'W
Trilogy Seep C	178°	34° 23.634'N, 119° 52.702'W
Trilogy Seep B	178°	34° 23.620'N, 119° 52.709'W
Trilogy Seep A	178°	34° 23.603'N, 119° 52.699'W
Patch Seep	140°	34° 21.850'N, 119° 49.755'W
Shane Seep	230°	34° 24.370'N, 119° 53.428'W
IV Super Seep	146°	34° 24.090'N, 119° 52.066'W
Tonya Seep	184°	34° 24.043'N, 119° 52.841'W
Horseshoe Seep	186°	34° 23.799'N, 119° 52.519'W
Rostöcker Seep	99°	34° 24.230'N, 119° 50.438'W
Seadog Seep	240°	34° 24.172'N, 119° 54.374'W

*θ – direction from West Campus Station (34.414949°N, 119.879690°W).

S3 Sonar return

The Sept. 2005 seep field survey sonar return, ω, was gridded at spatial resolutions from 11 to 225 m (Fig. S3) in a coordinate system with units of meters, centered on West Campus Station, WCS (34° 24.8969'N, 119° 52.7814'W). See Leifer et al. (2010) for details on the sonar survey data acquisition and analysis. Gridding involves averaging all ω values in each bin followed by a gap-filling low-pass filter. To gap fill, the center bin in a rolling 3x3-bin window which is empty, is replaced by the mean if there are more than 5 non-empty bins in the window. A hybrid 56/22-m gridding scheme gap filled the 22-m grid with the 56-m grid and was used in simulations (Fig. S3C).

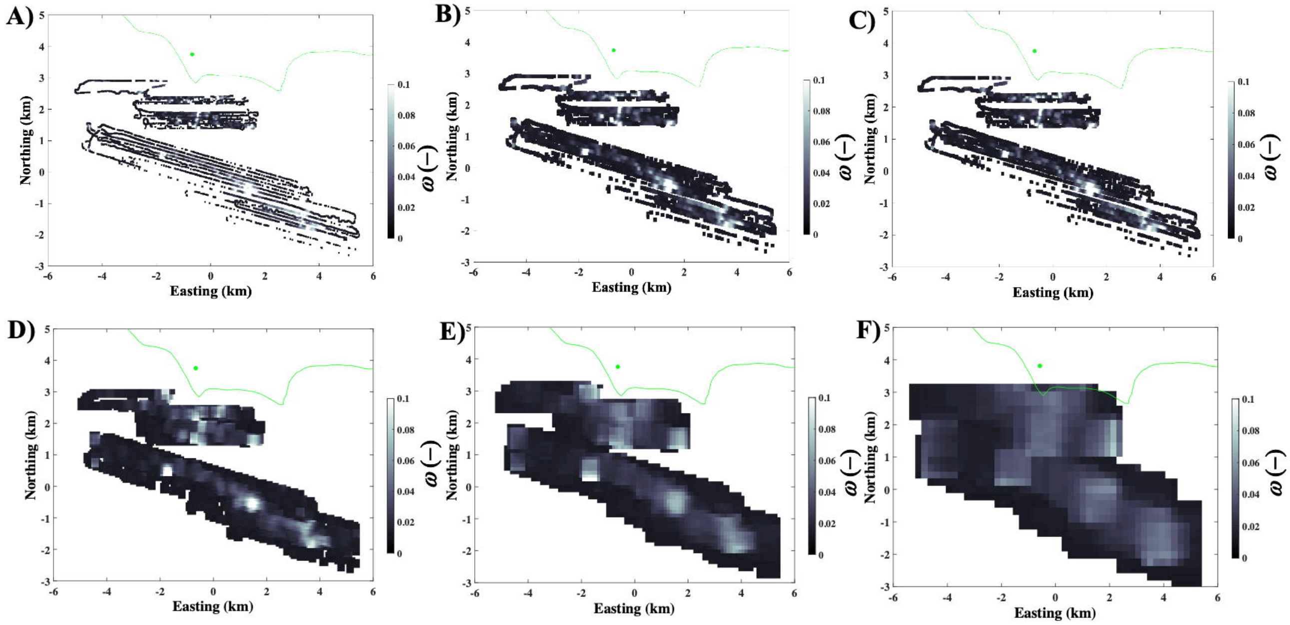

Figure S3: Sonar return, *ω*, maps for gridding at A) 11-m, B) 22 m, C) 22/56-m D), 56 m, E) 110 m, and F) 225 m. See text for details. Data key on panels.

The noise level was 0.015 and was identified from a histogram of *ω*, where the *ω* probability distribution shows a power law shift at the transition from seep distribution to noise domination (Fig. S4). Although there are seep emissions below the noise level, they cannot be segregated from noise and are neglected.

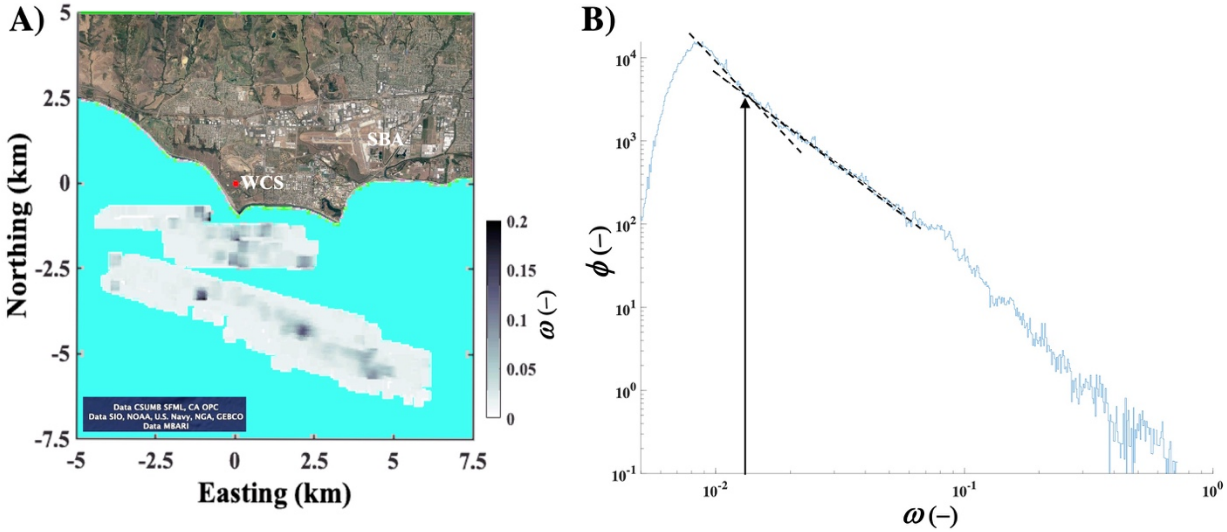

Figure S4: A) 22/56-m gridded 2005 sonar return, *ω*. Red dot shows West Campus Station (WCS) location. Shown in © GoogleEarth. B) Occurrence distribution, *ϕ*(*ω*). Arrow shows noise level based on shift in power law fits to *ϕ* at *ω*~0.015. Data key on panels. SBA - Santa Barbara Airport.

S4 Gaussian Plume model of an area plume

The model's core routines calculate a Gaussian plume (Eqn. 1) for the specified meteorological conditions in a Cartesian coordinate system (Fig. 5A). Then, the plume is rotated to the wind direction, re-gridded, and normalized to ensure mass conservation (Fig. S5B). The rotated plume is translated to each grid cell, scaled to emissions for that grid cell, and finally, all plumes are added (Fig. S5C). *C'* at WCS is calculated from the combined seep field emission plume map (Fig. S5D).

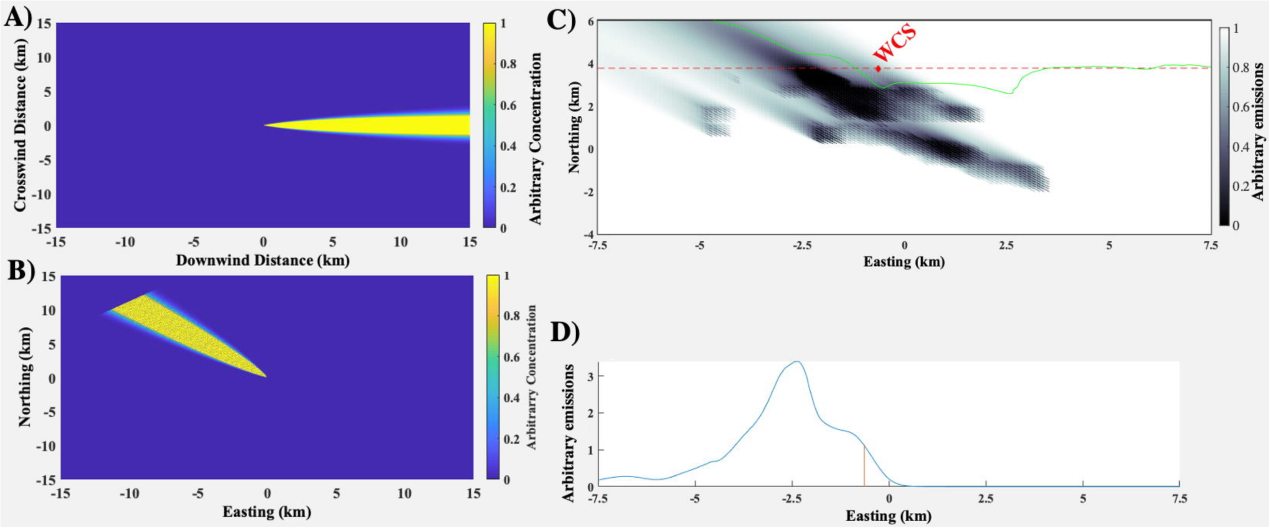

Figure S5: A) Gaussian plume concentration (arbitrary units) for 4 m s^{-1} wind speed and a 250-m thick boundary layer. B) Plume rotated to a wind direction, θ, of 135°, regridded, and normalized. C) Assembled plumes from all grid cells. Dashed red line shows a constant northing transect through West Campus Station, WCS. D) Concentration profile along WCS transect (dashed red line in panel C). Red dot shows location of WCS.

S5 Field atmospheric observations

Overall winds for 28 May 2016 were easterlies with modifications near the coast (Fig. S6). Winds in Goleta Bay included a strong onshore component, which was absent offshore Isla Vista where the shoreline features tall bluffs (~10-14 m). To the west of COP, winds had a strong offshore component as far west as halfway to Naples. Enhancements in the transect offshore west Sands Beach and Haskell Beach are consistent with emissions from seeps and/or abandoned oil wells in shallow waters, on the beaches, and/or from coastal onshore seepage.

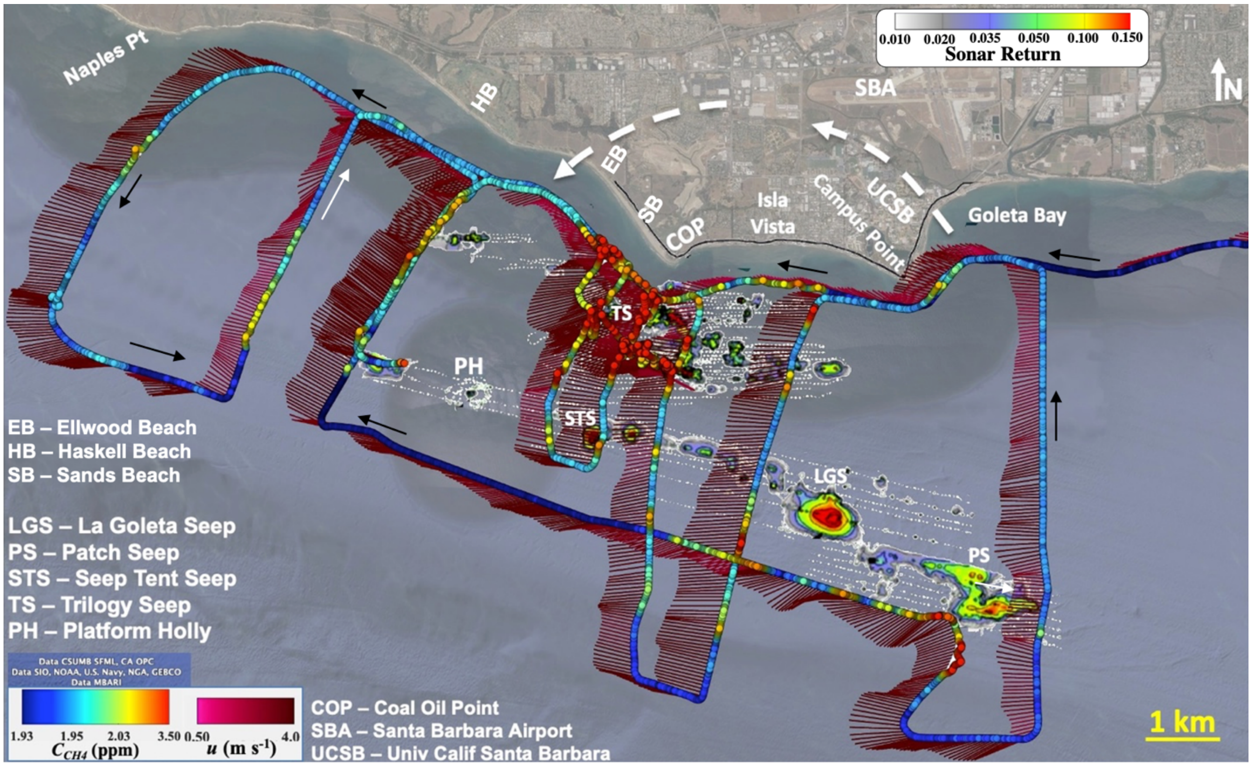

Figure S6: Methane, C_{CH4}, and wind, u, data for 28 May 2016. Sonar return map for reference shown on sea surface. Dashed white arrow shows proposed onshore winds; black arrows show travel direction. Shown in © Google Earth. Data key on figure. See Table S3 for locations of informally named seeps.

On 28 May 2016 winds were strongly from the east, which is uncommon (Fig. 5A) and largely overwhelmed the sea breeze. The easterly winds flow onshore in Goleta Bay and then offshore around Ellwood and Sands Beach, to the west of COP. This likely relates to a combination of the sea breeze in Goleta Bay and the overall easterly flow which in turn drives an offshore flow (by continuity) around Ellwood and Haskell Beaches. This wind flow creates strong convergence and divergence air flows.

S6 West Campus Station data

S6.1 Trends

WCS data show a significant change in 2008 when the station was upgraded from 1-hour to 1-minute time resolution, allowing far higher values of total hydrocarbon concentration, *THC*, and u (Fig. S7). Hereafter, all concentrations and emissions are *THC* unless otherwise noted. To assess whether the station upgrade introduced biases, the u and C probability distributions, $\phi(u)$ and $\phi(C)$, respectively, were compared for prior and post 2008 (Fig. S7C, S7D). The slopes of $\phi(u)$ with respect to u for 2 to 4 m s^{-1} are nearly identical for the prior- and post-2008 data, the main change is for highest and weakest u, i.e., the range was extended. Also, the slopes of $\phi(C)$ were very similar. Moreover, several shifts between subsequent years for u and C have been documented (1997 and 2012 for u, 1997 and 2013 for C), i.e., such shifts in annualized values are not unique to 2008 (Fig. S8). This strongly argues that the changes in average, median, and baseline values post 2008 were from better measurement of gusts and weak winds and short positive C anomalies.

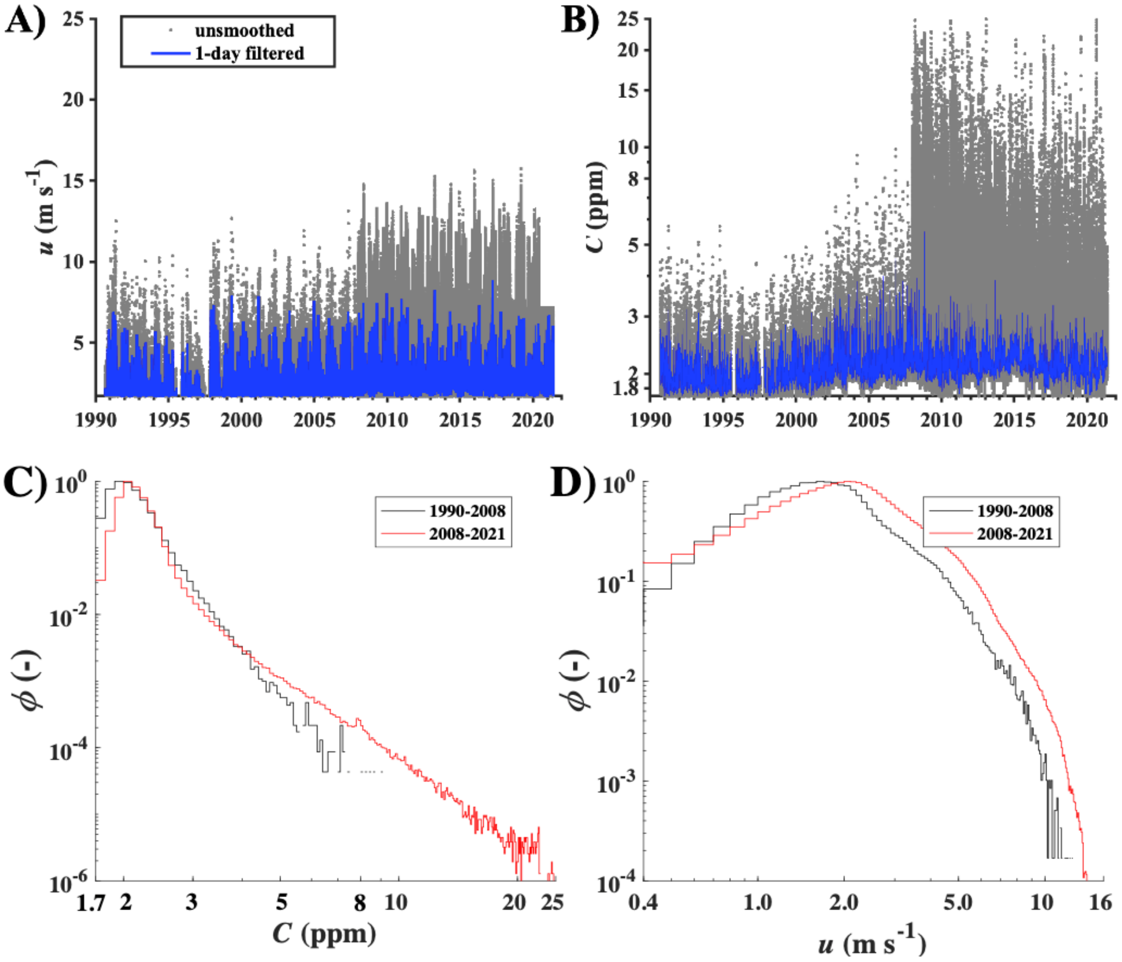

Figure S7: WCS unfiltered and 24-hour smoothed data for A) wind speed, u, and B) concentration, C. WCS concentration probability distribution, ϕ, for before and after the 2008 upgrade for C) u and D) C. Data key on panel.

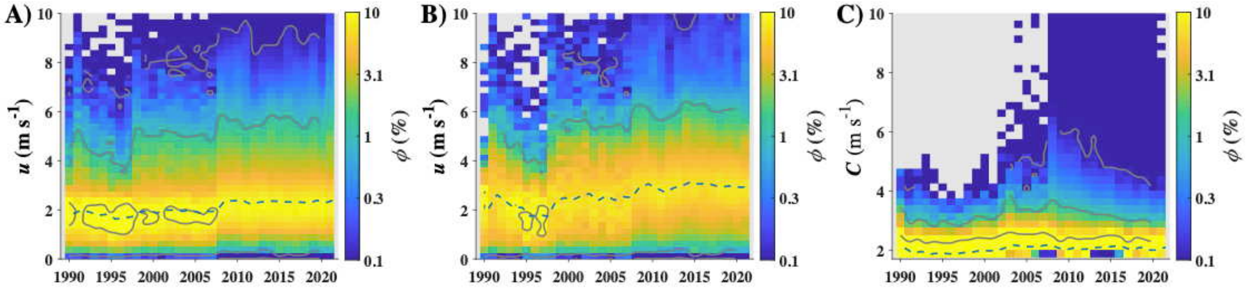

Figure S8: Annual wind speed, u, probability, $\phi(u)$, for A) all wind directions, θ, B) seep directions (135°<θ<270°). Contours at ϕ=0.1, 1, 10%, calculated from 4-year smoothed data. C) $\phi(C)$ for seep directions. Annual median (dashed line) shown on all panels. Data key for ϕ on figure.

A linear regression analysis of the wind data showed the median u increased at 0.023 m s^{-1} yr^{-1} and 0.04 m s^{-1} yr^{-1} for all directions and for seep directions, respectively (Fig. S9A). This corresponds to an increasing sea breeze (from the seep direction). Summer winds have increased faster than winter winds, 0.043 versus 0.027 m s^{-1}, respectively.

The residual, R, to the Gaussian fit to $C'(\theta)$ showed an overall increasing linear spatial trend of 0.17 ppb degree^{-1} from 175° to 210° (Fig. S9B). There is a peak at R~230° that corresponds to Shane Seep and a peak at R~170°, which does not correspond to any named seeps (Table S3), but is in the general direction of the inshore seep trend to the east of the Trilogy Seeps.

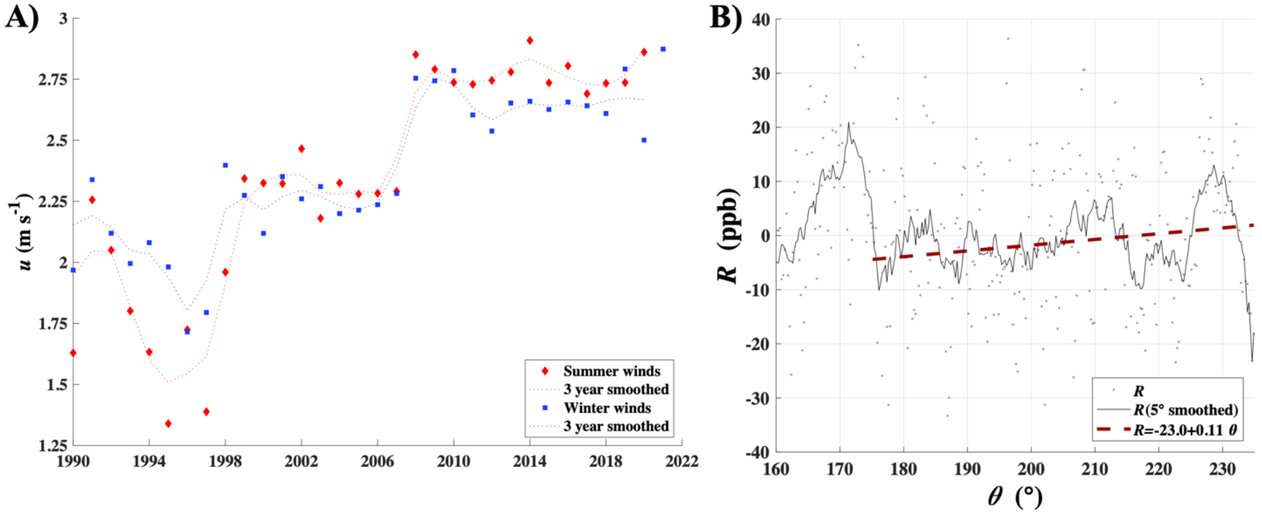

Figure S9: A) Seasonally-segregated, annually-averaged wind speed, u for WCS. Summer is for Julian days 135-250, winter is Julian days 260-130, and three-year rolling-average. B) Residual, R, to dual Gaussian plume fit (Fig. 4B) to wind-direction resolved concentration, $C(\theta)$, for 1990-2019 for unsmoothed, 5° smoothed, and least-squares, linear-regression analysis fit. Data key on panel.

S6.2 Diurnal

Hourly-segregated averaged *u* and *C* for 1991-2007 (Fig. S10) show similar overall patterns to 2008-2021 for the seep directions (Fig. 6). The station improvements shifted averages, making averaging the entire datasets inappropriate. One difference was the late-afternoon peak in *C* towards the east-northeast, which was absent in the earlier period. The significant expansion of housing and commercial developments in this direction in recent decades likely underlies this change.

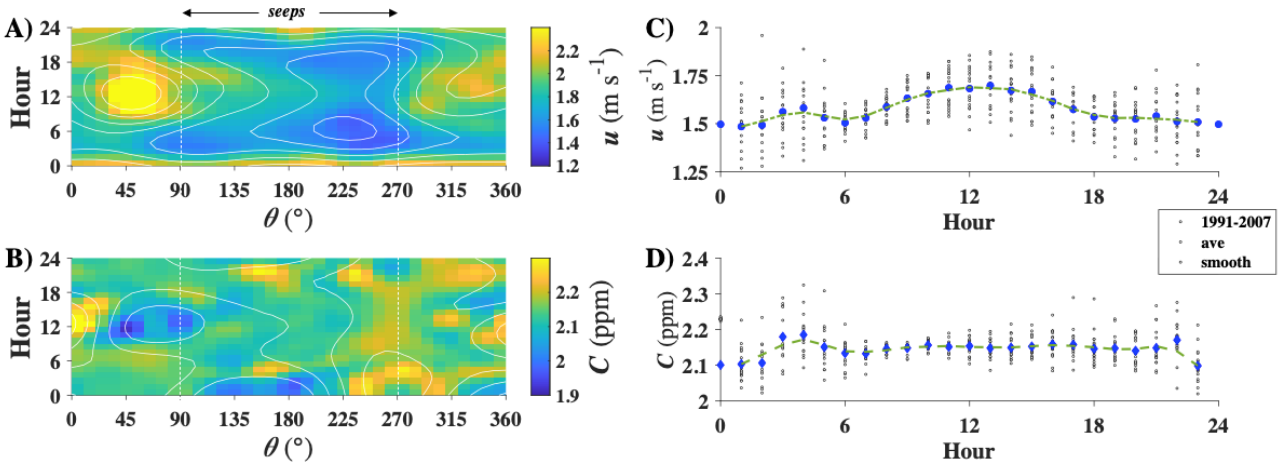

Figure S10: 1991-2007 hour- and wind direction-, θ, resolved A) wind speed, *u*, and B) concentration, *C*. C) Hourly-resolved, seep-direction (90–270°) *u*, and D) seep direction *C* averaged, individual years, and 3-year smoothed. Data key on figure. Midnight data missing due to daily calibration.

S7 Seep field emissions

S7.1 Effect of model wind direction resolution

Emissions simulations are run iteratively, initialized by the sonar distribution, which was multiplied by a scaling factor, $K(\theta)$, initialized with $K(\theta)$=22,620, which was applied to $E_A(x,y)$. Notably, the θ-resolved C'_{Sim} and C'_{Obs} disagree significantly, which is unsurprising as the relationship between ω and seabed emissions is complex (Leifer et al., 2017) with additional complexity arising from transport across the water column. For sensitivity studies, the scaling factor, $K(\theta)$, see Eqn. 3, was applied to $E_A(\theta)$ after each iteration until convergence (<1%), typically within 5 iterations (Fig. S11).

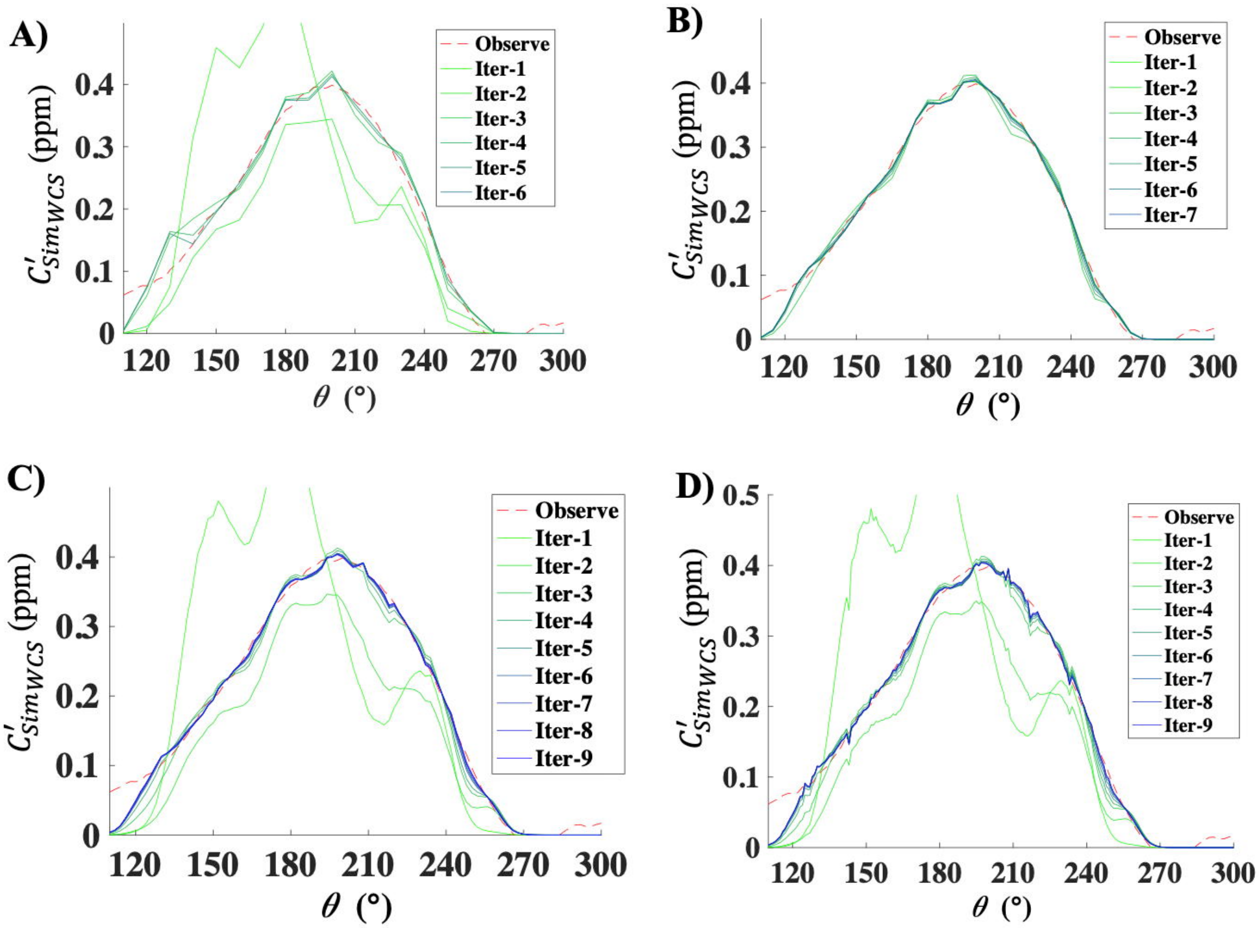

Figure S11: Observed and simulated WCS concentration anomaly, C'_{Obs} and C'_{Sim}, respectively, versus wind direction, θ, for all iterations for 22/56-m sonar map and angular, θ, resolutions, of A) 10°, B) 5°, C) 2°, and D) 1°. Data key on figure.

Simulations were conducted with no distance correction, i.e., $K(r,\theta)$ =1 for north offsets of WCS location, Y, from 0 to 3 km. For reference, the inner and outer seep trends are 1.5 and 3.5 km from WCS at their closest distance. Simulations showed a near linear response in E_A to Y (Fig. S12), which was applied to as a linear distance weighting function, $K(r,\theta)$, in all further simulations.

S7.2 Effect of distance to seep field on emissions

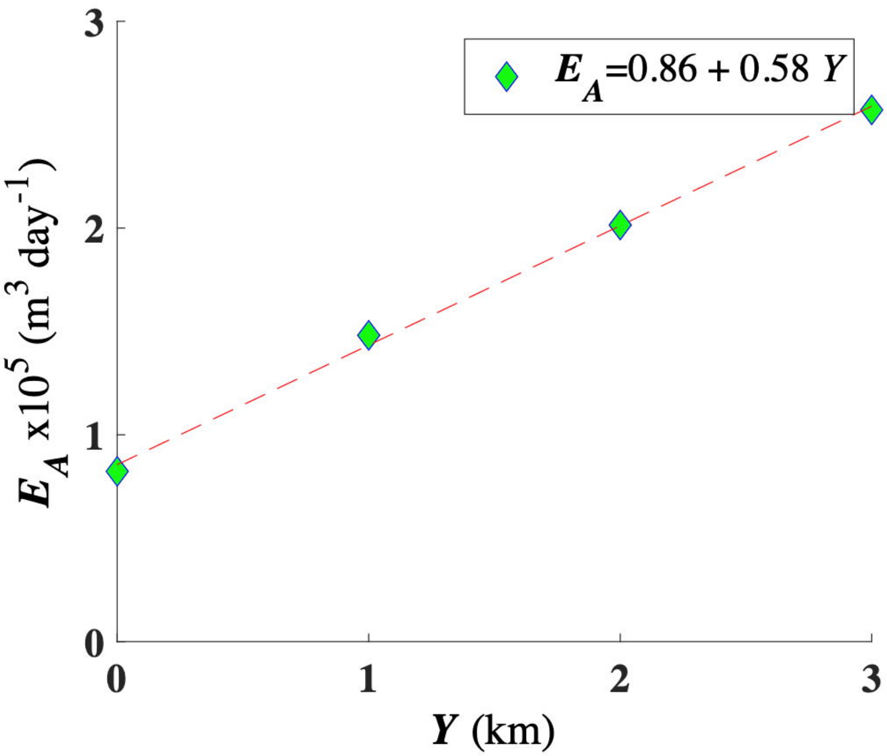

Figure S12: Simulated atmospheric emissions, E_A, with respect to north offset, Y, modeled with no distance varying correction factor, and linear fit shown on panel.

S7.3 Sonar return versus atmospheric emissions

Plotting all E_A versus ω shows a non-linear relationship (Fig. S13) with E_A increasing very steeply with ω before rolling over for values of E_A in the range 1-10 g s^{-1} m^{-2}. After rolling over, there were several populations of ω-values that increased as a power law with an exponent slightly less than unity. Emissions are the fraction of the seabed emissions that are transferred into the atmosphere, including from adjacent pixels where emissions are from evasion – the simulation was initialized with non-zero ω in neighboring cells to allow the simulation to infer sear-air gas evasion emissions from these cells. This accounts for values of ω less than 0.02 in Fig. S13. The highest ω corresponds to the strongest plumes where sonar tends to saturate (Leifer et al., 2017) but dissolved gas evasion emissions to the atmosphere are more efficient due to the strong upwelling flow in strong plumes.

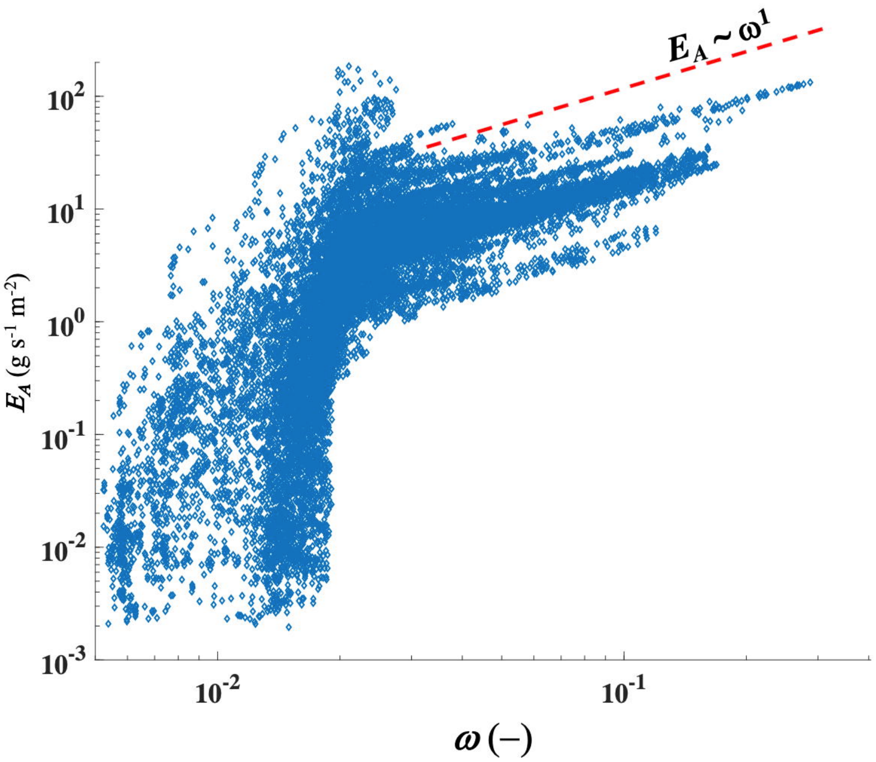

Figure S13: Sonar return, ω, versus derived atmospheric emissions, E_A. Line illustrates unity power law.

S7.4 Emissions Uncertainty

S7.4.1 Angular resolution

Sensitivity to angular resolution, $\delta\theta$, is very weak, <1% in E_A for corresponding to an increase in angular resolution, $\delta\theta$, from 10° to 1°. For example, reducing $\delta\theta$ from 2° to 1° only changed E by 0.3%. $\delta\theta$ resolution affects simulation resolution with coarse resolution blurring the fine-scale sonar structure that is apparent in the 1° simulations (Fig. S11D). Note, $\delta\theta$=1° simulations produced overly-quantized results for the hybrid 22/56-m sonar maps including banding artifacts, i.e., sonar resolution limitation (Supp. Fig. S3). Thus, $\delta\theta$ was 2° outside of specific sensitivity simulations.

S7.4.2 Veering

Veering, ψ, was implemented by adding ψ to θ in the calculation of $K(r,\theta)$, i.e., $K(r,\theta+\psi)$. The effect of wind veering was most strongly apparent at the field's edges (Supp. Fig. S14). ψ =+10° produced better overall spatial agreement with the sonar map, e.g., better representation of the relative importance of La Goleta Seep compared to the no wind veering simulation, while also lessening the enhancement of the western seep field's edge (Fig. 7B).

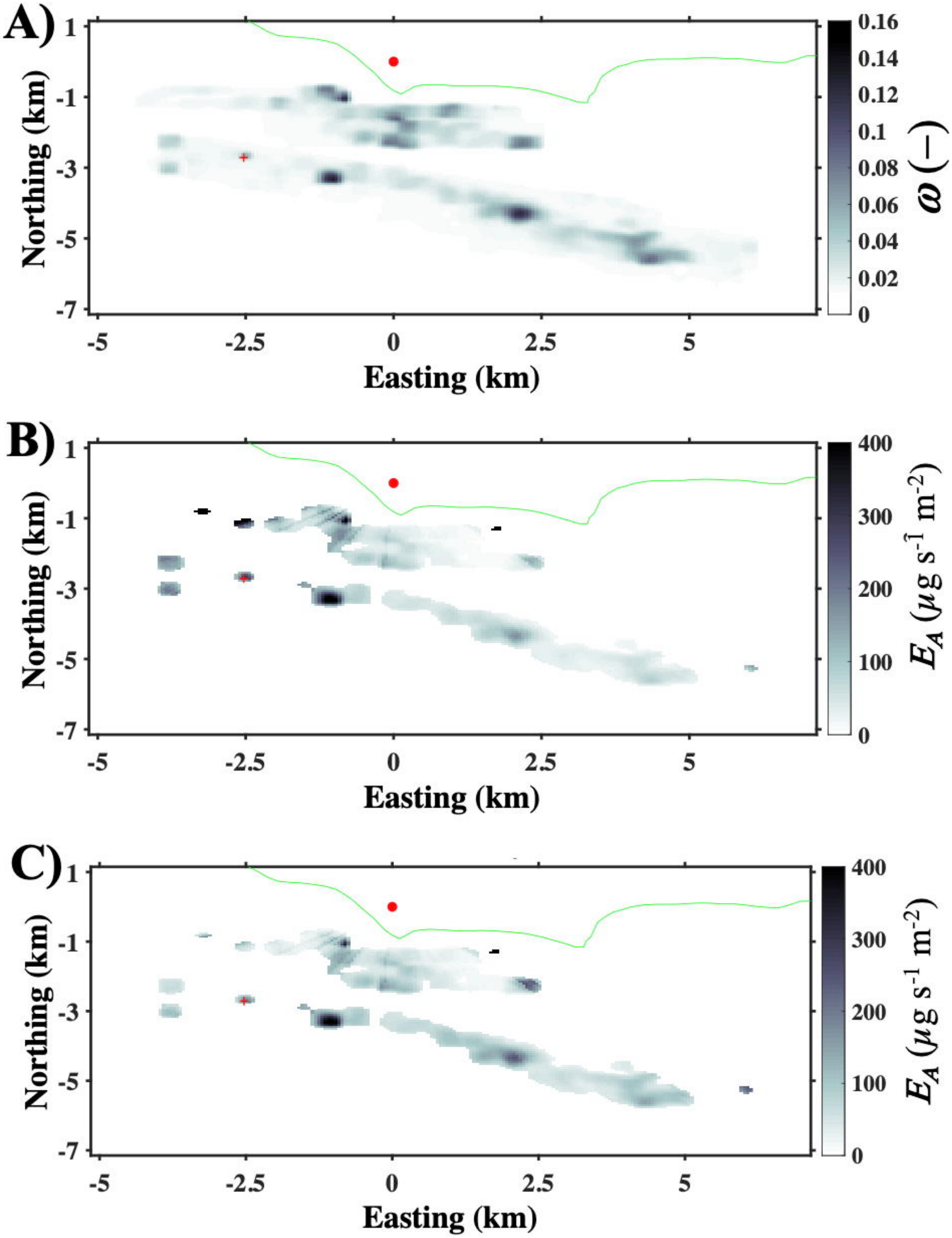

Figure S14: A) Sonar return, ω, map gridded to 56-m resolution. B) Atmospheric emissions, E_A, map for wind veering, ψ, of B) ψ=-10° and C) ψ=10°. Data key on figure.

Wind veering simulations overly emphasized emissions at the seep field's edge towards the veering direction, although even the no-wind veering simulation emphasized the western field's seepage. This suggests wind veering across the field was likely not constant – a reasonable hypothesis given the shifts of the coastline in the area of the field.

E_A was very weakly sensitive to ψ, with ±10° veering corresponding to only a few percent in E_A. This low sensitivity arises because ψ simply shifts emissions to neighboring cells, only changing E_A when neighboring cells have no seepage, which forces the model to increase emissions from cells on the other seep trend.

S7.4.3 Wind speed

There is a strong sensitivity of E_A to u, particularly for small negative decreases in u, although sensitivity saturated at +10%/-20% (Fig. 9B). The underlying factor to this sensitivity was investigated in a series of non-iterative simulations of $C'(\theta)$ for a range of u, which showed variations were most strong for very weak wind speeds (Fig. S15A). Simulations spanned the range of observed u. Instrumentation uncertainty in u is a few percent, thus uncertainty in u arises if WCS winds are unrepresentative due to acceleration or deceleration between the seep field and WCS. C' is highest for $u = 1$ m s^{-1}, which is weaker than actual winds, whereas C' for $u = 8$ m s^{-1} is about a tenth C' for $u = 1$ m s^{-1}. At lower u, plume disperse more laterally, "blurring" structures than at higher u. Note, u and BL are not independent – by continuity, an increase in u – i.e., acceleration, requires a decrease in BL. Thus, BL sensitivity largely counters u sensitivity, discussed in Sec. S7.4.4.

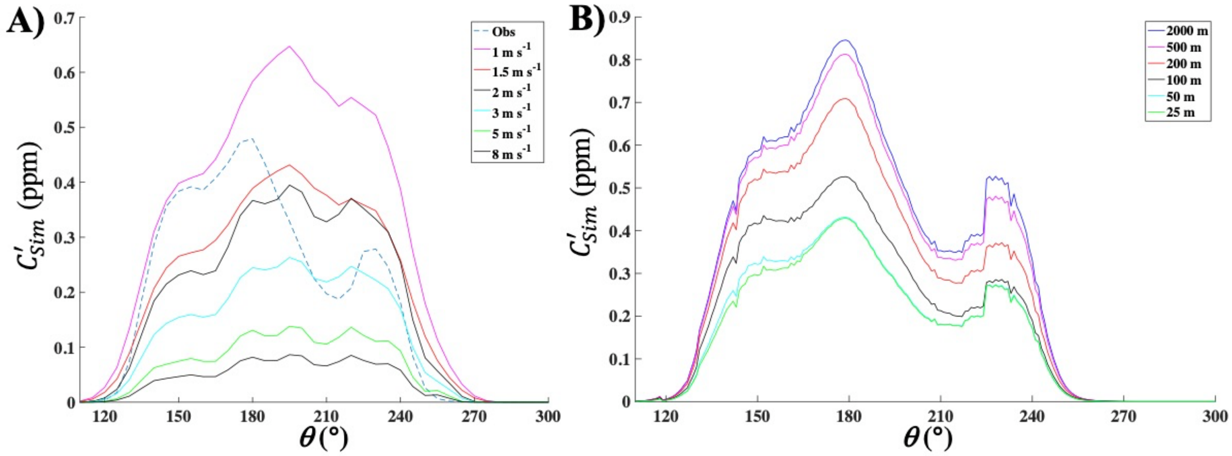

Figure S15: Simulated concentration anomaly, C'_{Sim}, versus wind direction, θ, for WCS for different **A)** wind speed, u, including the observed $u(\theta)$. **B)** Boundary layer height. $\delta\theta$ resolution is 1°. Data key on figure.

S7.4.4 Boundary layer

BL sensitivity is weakly non-linear and weak - a 40% decrease in *BL* (250 to 150 m) only decreased E_A by 17%, less so for a 100 m increase to 350 m in *BL* (Figs. 9D, S15B). The effect of large *BL* changes saturates – for very high *BL*, it has no effect, whereas for very shallow *BL*, multiple reflections homogenize the boundary layer leaving only dilution (i.e., u) driving *BL* sensitivity. Thus, variations in *BL* of a factor of 40 correspond to a factor of 2 change in $C'(\theta)$. Although the nocturnal *BL* is significantly shallower, nocturnal winds largely are the (northerly) land breeze and thus uncommon for the seep direction and not relevant to the simulations. *BL* values for the seep field and WCS have not been studied, thus, a 2nd-order polynomial was fit to *BL* versus E_A and averaged (absolute) over possible ranges. For $200<BL<300$ m, the mean absolute value was 3%, for $150<BL<350$ m it was 6%.

S7.4.5 Concentration

E_A sensitivity to C' is weaker than that of u, particularly for small variations, and is linear (Fig. 9). Uncertainty in C arises from flame ion detector drift between nightly calibrations. Thus, the difference in concentration before and after calibration is the daily drift as well as any changes in ambient, which should on average be zero, particularly for around midnight when the atmosphere is stable. A 500-point histogram of the total daily drift was calculated and values <±0.2 ppb were fit with a Gaussian function (larger deviations exhibited a broader distribution which, likely resulted from ambient trends) and found a half-width of 170 ppb, or ±85ppb. Thus, the average drift is ~40 ppb dy^{-1}, reduced for annualized values to ~2 ppb dy^{-1} ($1/\sqrt{365}$), i.e., <1% of the C' value of 300 ppb. As such, uncertainty in C' is not a significant contributor to uncertainty in E_A.

S7.4.6 Combined wind and boundary layer

E_A sensitivity to *BL* largely counters E_A sensitivity to u (Fig. 9B, 9D**)**, even when mismatched – a ±40% decrease in *BL* and ±20% increase in u corresponds to 6% and 9% decreases in E_A, i.e., less than half the mismatch. By continuity, this should be quite small, reflecting lesser changes from pressure, temperature, and topographic forcing. Underlying this weak sensitivity is that the linear sensitivity of E_A to u largely arises from dilution – higher u dilutes the plume more. This counters the effect of *BL* on E_A, which by continuity implies that higher *BL* corresponds to a slower u, whereas a lower BL corresponds to a higher u. Note, this weak sensitivity is for a change in BL from the offshore to onshore and the resultant change on winds, not a change in the overall (regional) BL.

S7.4.7 Inshore / offshore partitioning

The model cannot determine how to apportion emissions between the inshore and offshore seeps. Simulations found a complex relationship between E_A and ζ (Fig. 9F) because simulations re-assign some emissions between the seep trends depending on the presence or absence of seepage for θ where there is no seepage on one of the two trends (Fig. S16). As such, a potentially strong sensitivity arises from the partitioning with respect to θ between the offshore and onshore seepage trend. Initial simulations used a uniform distance partitioning, $K(r)=1$, that unrealistically increased inshore seepage compared to ω. Based on the northing offset simulations a linear function was used for $K(r)\sim r$, which did not increase inshore seepage compared to ω. This argument notes that whatever the functional relationship between E_A and ω is, similar ω implies similar E_A, and thus the similarity in the ω probability distribution between the inshore and offshore trends implies a rough similarity in the E_A probability distribution (Fig. 8).

Sensitivity simulations were run for various shifts in the relative emissions from the inshore and offshore trends – i.e., for +10% inshore -10% offshore, while maintaining a linear variation in $K(r,\theta)$. Sensitivity is strong, and complex – interestingly, reversing between -10° and 10°. This behavior is due to shifting emissions onto different seep areas in the inshore or offshore seep area. For $-30\% < \zeta < +25\%$, uncertainty ranges from -10% to +5%. Although higher changes in ζ are certainly feasible, both seep trends source from the same formation, which means on a multidecadal timescale, changes in one seep trend likely reflect changes in both seep trends.

Additionally, seepage could shift within the trends – nearer or further – which was assessed by the simulations of north shifts of WCS (Fig. S12). Total trend widths are ~300 m for the offshore and 600 m for the inshore, or an average distance deviation of ±75 and ±150 m, corresponding to E_A variations of a few percent at maximum deviation, and less when spatially averaged over the limits.

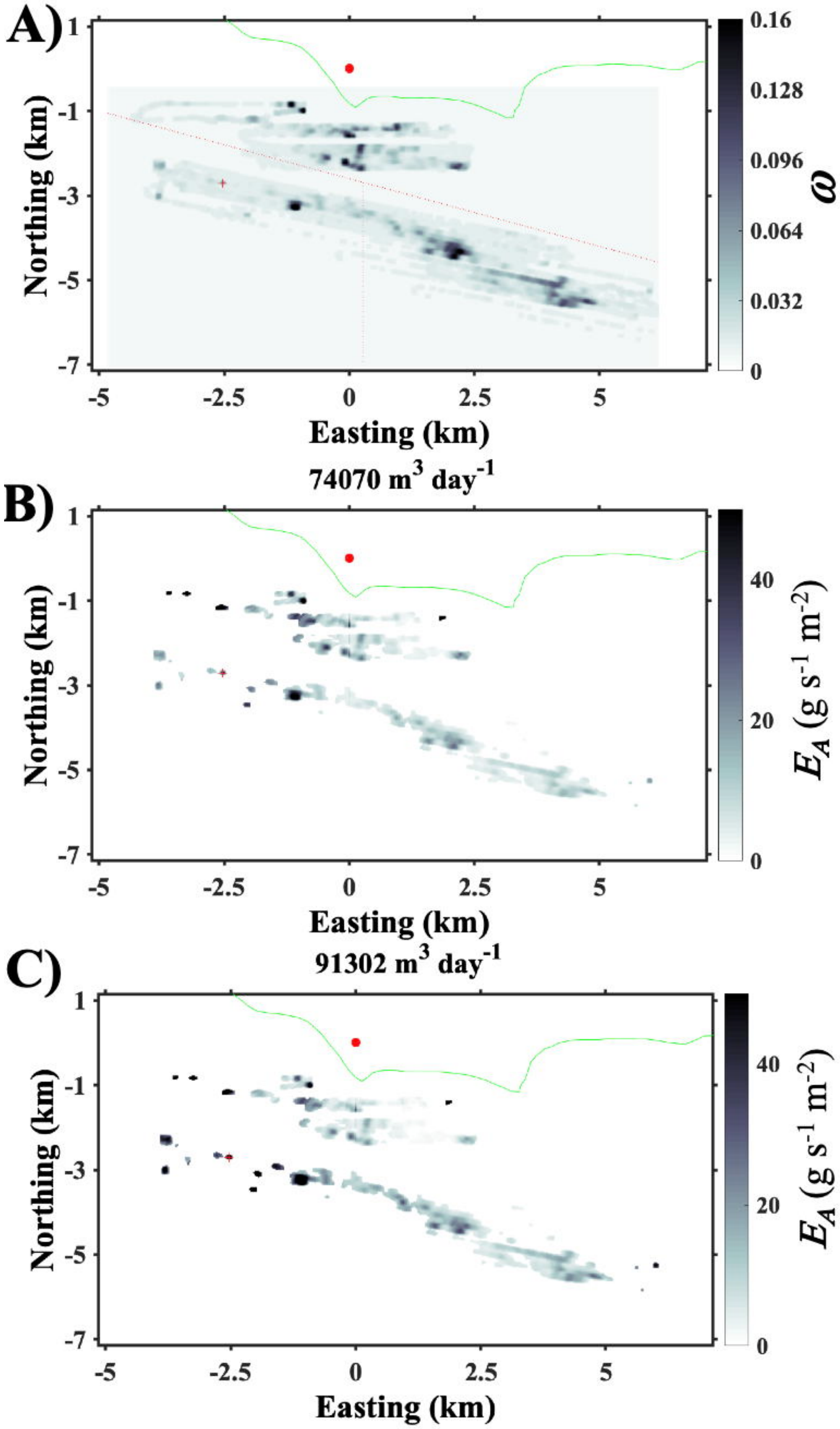

Figure S16: A) Sonar return, ω, map gridded to 56/22-m resolution. Atmospheric emissions, E_A, for inshore/offshore trends relative enhancement, ζ, for B) ζ=-25% and C) ζ=+25% offshore enhancement.

S8 Future data needs and model improvements

S8.1 Key data needs

The largest driver of uncertainty was whether emissions arose from the inshore or offshore seep trends, which could not be determined from WCS data. An approach to address this would be a second air quality station located towards the seep field's east side, which would allow triangulation. If the station included a ceilometer, it could measure *BL*, and provide an estimate of this uncertainty in E_A. Long-term *BL* data would characterize the relationship between *BL* and solar insolation, diurnal cycle, and winds, allowing application to historical data.

Additionally, *THC* is a less than ideal seep emission indicator as it can arise from other sources, such as motor vehicles or fires. Thus, speciation would improve significantly the ability to interpret WCS data, ideally a combination of CEAS analyzers and a gas chromatograph.

WCS data poorly constrains the diurnal cycle given that the typical diurnal cycle of strengthening winds in the afternoon also shifts towards westerlies, with seep field emissions bypassing WCS. Given that an atmospheric plume survey can derive emissions in a couple of minutes, multiple seep areas should be repeat surveyed from morning through early evening to characterize the relationship between wind speed, wave development, and emissions, and if possible, the plume from the entire seep field.

The study focus was marine seepage, and thus it neglected terrestrial seepage; however, the data analysis demonstrated that there are notable terrestrial emissions. Further WCS data analysis should include assessment of Ellwood Field emissions with onshore surveys searching for seep emissions in neighborhoods by measuring seep gases downwind of faults and also abandoned wells, particularly those that intersect with the Ellwood Field.

Finally, the downcurrent dissolved plume's fate is poorly understood as there is an absence of field data collected under typical afternoon (strong, prevailing) winds. A combination of field data collected downwind of the downcurrent plume, ideally in conjunction with water sampling, and further modeling of WCS data can help constrain this source, better characterizing the fate of COP seep field emissions.

S8.2 Model improvements

The area plume inversion model was used to derive emissions on the field and sector scales. Efforts to derive emissions at finer spatial scales were stymied by uncertainty in wind veering. At the field scale, there was very weak sensitivity of E_A to wind veering (Fig. S14); however, simulations without wind veering shifted emissions off of important seeps like Trilogy Seep to nearby, much smaller, seeps. Additionally, the model assigned emissions to both field edges. This suggests that wind veering varies with wind direction – consistent with existing (admittedly limited) field observations, i.e., wind veering for the southeast and southwest are different. This is not surprising given the different orientations of the coast on the east and west sides of COP, as well as the topography between WCS and the coast with bluffs (~20 m) on the east side, which are lacking to the west (Sands Beach). Wind veering likely decreases further offshore aligning more with prevailing winds. Additionally, the wind field likely becomes more uniform across the field. Further field observations are needed to correctly characterize and incorporate wind veering to allow simulations to characterize changes in emissions from different areas of the field.

The model's enhancement of seepage at both seep field's edges likely arises both from wind veering and from outgassing from downcurrent plumes. Currently, outgassing in the seep field area is assigned to the nearest seep area along the wind direction. This causes a problem for wind directions in the seep field without mapped seepage in that direction, including beyond the seep field edges.

Attempts to uniformly assign emissions with distance – i.e., no preferences – led to an unrealistic shift of emissions to the inshore seeps (based on a relative sonar return). One improved approach would be to apply the linear distance correction where the relative seep strength in the two trends for a wind direction are comparable (as in this study), but to prioritize the major seepage over minor seepage in either seep trend where the relative strengths are disparate.

Several model improvements were not implemented due to computational limits – current simulations take multiple days on a fast workstation (16-core PowerMac, 96 GB RAM, 3.4 GHz). For example, rather than simulating the mean value of winds in a direction, the probability distribution of u in each wind direction (e.g., Fig. 5A) could be used, calculating a wind-weighted concentration for comparison with the observed concentration at WCS. This would significantly increase computational load. An additional improvement would be to include a boundary layer height that varied with wind speed and the diurnal cycle, and turbulence parameterizations that are based on solar insolation. Finally, higher angular resolution and sonar map resolution (doing one without the other causes non-physical striation) improves the ability to capture changes at different seep areas, but the increased angular resolution introduces more gaps in the seep emissions source function. This could be addressed by adding a "dispersed" source of sea-air gas evasion that follows currents from the seep areas.

Table of Nomenclature

THC	Total hydrocarbon
C_{CH4}	Methane concentration
$C'_{Obs}(\theta)$	Wind direction-resolved WCS observed concentration
$C'_{Sim}(\theta)$	Wind direction-resolved WCS simulated concentration
a, b, c	Atmospheric turbulence parameterizations
BL	Boundary layer height
C	Concentration
C'	Plume (anomaly) concentration
E_A	Atmospheric emissions
$E_A(i, j)$	Grid cell i, j atmospheric emissions
h	Plume emission height in the Gaussian Plume model
i	Grid cell easting index
I	Solar insolation
j	Grid cell northing index
$K(r,\theta)$	Wind direction and distance-resolved correction function to emissions
$K(\rho)$	Distance correction function to emissions
n	exponent in σ_z parameterization
r	Distance from WCS to cell i, j
R	Residual in C' after Gaussian functional fit
u	Wind speed
$u(\theta)$	Wind direction-resolved wind speed
x, y, z	Cartesian coordinate system in wind reference frame
Y	Northing offset of WCS
$\delta\theta$	Model wind direction angular resolution
$\phi(C)$	Concentration probability distribution
$\phi(u)$	Wind probability distribution
θ	Wind direction
σ_y, σ_z	Turbulence parameterizations in the Gaussian plume model
ω	Sonar return
ψ	Wind veering
ζ	Relative inshore and offshore emissions

Supplemental References

Briggs, G. A. (1973). Diffusion estimation for small emissions, NOAA, Air Resources Atmospheric Turbulence and Diffusion Laboratory, Oak Ridge, Tennessee, 87-147.

Hanna, S. R., Briggs, G. A., and Hosker Jr. (1982). R. P., Smith, J. S. (Ed.): Handbook on Atmospheric Diffusion, Technical Information Center, U.S. Department of Energy, 110 pp.

Leifer, I., Chernykh, D., Shakhova, N., and Semiletov, I. (2017). Sonar gas flux estimation by bubble insonification: Application to methane bubble flux from seep areas in the outer Laptev Sea, The Cryosphere, 11, 1333-1350, doi:10.5194/tc-11-1333-2017.

Leifer, I., Kamerling, M., Luyendyk, B. P., and Wilson, D. (2010). Geologic control of natural marine hydrocarbon seep emissions, Coal Oil Point seep field, California, Geo-Marine Letters, 30, 331-338, doi:10.1007/s00367-010-0188-9.

Leifer, I., Melton, C., Frash, J., Fischer, M. L., Cui, X., Murray, J. J., and Green, D. S. (2016). Fusion of mobile in situ and satellite remote sensing observations of chemical release emissions to improve disaster response, Frontiers in Science, 4, 1-14, doi:10.3389/fenvs.2016.00059.